J Nanostruct 14(2): 452-465, Spring 2024

RESEARCH PAPER

Synergistic Effects of Ni-doped Co_3O_4 Coupled with ZnO Nanoparticles for Enhanced Photocatalytic Decolorization of Reactive Red 141 Dye

Abbas Sadeghzadeh-Attar

Department of Metallurgy and Materials Engineering, University of Kashan, Kashan, Iran

ARTICLE INFO

Article History:
Received 12 January 2024
Accepted 24 March 2024
Published 01 April 2024

Keywords:
Decolorization
Photocatalytic
Reactive red 141 dye
ZnO/Ni-doped Co_3O_4 nanocomposite

ABSTRACT

Developing high-performance photocatalytic materials to remove contaminants from water sources is vital for health and environmental conservation. In this study, ZnO/Ni-doped Co_3O_4 heterojunction nanocomposites were successfully fabricated by sol-gel method and utilized as one of the most promising photocatalysts for the photocatalytic decolorization of reactive red 141 (RR141) dye. The concentration of Ni dopant was selected from 0 to 8 wt%. The prepared photocatalysts were characterized by X-ray diffraction (XRD) and field emission-scanning electron microscope (FE-SEM), energy dispersive X-ray spectra (EDS), and UV-visible diffuse reflectance spectra (UV-vis DRS) analysis. The optical band gap of ZnO nanoparticles, Co_3O_4 nanoparticles, ZnO/Co_3O_4, ZnO/2Ni-Co_3O_4, ZnO/5Ni-Co_3O_4, and ZnO/8Ni-Co_3O_4 nanocomposites was found to be 3.25, 2.54, 2.9, 3.78, 2.71, and 2.56 eV, respectively. The photocatalytic results demonstrated robust performance for ZnO/5Ni-Co_3O_4 nanocomposite in the decolorization of RR141 dye, achieving output as high as 97.4% under 100 min light irradiation. This enhanced photocatalytic efficiency can be attributed to the synergistic effects of Ni doping into Co_3O_4 lattice and its coupling with ZnO to form an n-p heterojunction ZnO/Ni-Co_3O_4 nanocomposite, which effectively improves light absorption and separates photogenerated charge carriers on the surface of the nanocomposite.

How to cite this article
Sadeghzadeh-Attar A. Synergistic Effects of Ni-doped Co_3O_4 Coupled with ZnO Nanoparticles for Enhanced Photocatalytic Decolorization of Reactive Red 141 Dye. J Nanostruct, 2024; 14(2):452-465. DOI: 10.22052/JNS.2024.02.008

INTRODUCTION

Synthetic dyes as one of the organic compounds released from various chemical industries such as textile, pigment, food, and cosmetics, are hazardous organic pollutants that have caused severe threats to both human health and the environment [1]. Even low dye concentrations contaminated in effluents may cause mutagenesis and carcinogenesis, and block the ecosystem [2]. Anionic reactive dyes, comprising reactive red 141 (RR141) dye are complex, very stable and resistant to decolorization due to their aromatic anthraquinone structure with high molecular weight [3]. Hence, developing an efficient and cost-effective technology to promptly eliminate these harmful dyes in wastewater is essential. So far, several methods, including biosorption [4], active carbon adsorption [5], Fenton-like oxidation

* *Corresponding Author Email: sadeghzadeh@kashanu.ac.ir*

[6], photocatalytic [7], and electrocoagulation [8], have been studied to remove dye pollution from industrial wastewater. Most of the mentioned methods generally have drawbacks for dye elimination, which limit their applications. Recently, the photocatalytic process as a new approach has been adopted and gained extensive attention. It offers the advantages of economy, high efficiency in decolorizing the dyes without producing harmful products, and environmental friendliness [9]. Numerous semiconducting photocatalysts are utilized to decolorize dyes such as SnO_2 [10], TiO_2 [11], ZnO [12], Ag_3PO_4 [13], and $BiVO_4$ [14]. Among them, ZnO is generally an appropriate candidate owing to its non-toxic nature, chemical stability, photostability, abundance, cost effectiveness, eco-friendliness, suitable band gap (around 3.0 eV), strong oxidation capability, and potential photocatalytic efficiency [15-17], which acts as a superior photocatalyst material for the degradation of dye pollutants. Unfortunately, because of the wide bandgap, ZnO can only be excited under UV light, which is a small fraction of sunlight (3-5%) [18]. Besides, the high recombination rate of photoinduced electron-hole pairs greatly limited the photocatalytic efficiency of ZnO [19]. Some approaches have been developed to solve these deficiencies, such as noble metal deposition [20], element doping [21], and coupling with narrow band gap semiconductors to form binary or trinary heterojunctions [22, 23]. Among the narrow band gap materials, Co_3O_4, a p-type semiconductor has been widely studied for the photocatalytic degradation of dyes because of its absorption capability of visible light and valence band potential being close to the conduction band potential of ZnO. Hence, it creates a suitable heterojunction with ZnO for the maximum photocatalytic application [24]. The rapid recombination of charge carriers has reduced the photocatalytic efficiency of Co_3O_4, which can be partially modified by introducing doping elements to the Co_3O_4 lattice [25]. Recently, Abo Zeid et al. [26] reported that Ni-, Cu, Ni- and Cd, Ni-doped Co_3O_4 nanoparticles show much higher photocatalytic efficiency for the degradation of methyl orange dye than that of pure Co_3O_4. Keerthana et al. [27] synthesized 1 M Sn-doped Co_3O_4 nanoparticles for the photocatalytic degradation of methylene blue dye under visible light. Fida et al. [28] successfully doped Co_3O_4 with Mn, a composite of carbon nanotubes via co-precipitation. Herein, binary ZnO/Ni-Co_3O_4 nanocomposites have been successfully fabricated and the synergistic effects of Ni-doped Co_3O_4 coupled with ZnO nanoparticles was investigated to photocatalytic decolorization of reactive red 141 dye. The prepared heterojunction exhibited enhanced photocatalytic activity compared with single ZnO and Co_3O_4 nanoparticles. The probable photocatalytic mechanism of ZnO/Ni-Co_3O_4 nanocomposite under tungsten lamp irradiation was also discussed.

MATERIALS AND METHODS

Synthesis of ZnO/Ni-doped Co_3O_4 nanocomposite

In the present work, a sol-gel process operating at air atmospheric was employed to synthesize ZnO/Ni-doped Co_3O_4 nanocomposite. All chemical reagents were purchased from Sigma-Aldrich and used without further purification. To prepare a 0.25 M solution of pure Co_3O_4, 1.8 g hexahydrate nitrate cobalt ($Co(NO_3)_2{\cdot}6H_2O$; 99%) and 3.4 g urea ($CO(NH_2)_2$; 97%) were dissolved in 30 mL of water and stirred magnetically for 30 min. To obtain Ni-doping, hexahydrate nickel nitrate ($Ni(NO_3)_3{\cdot}6H_2O$; 97%) was added to the precursor solution with different amounts (2, 5, and 8 wt%) for all doped samples. The crystalline Fe-doped Co_3O_4 nanoparticles were obtained after drying at room temperature and then calcination at 400 °C for 3 h. To synthesize ZnO nanoparticles, 2.2 g of zinc nitrate hexahydrate ($Zn(NO_3)_2{\cdot}6H_2O$; 98%) was dissolved in 40 mL of DI water and stirred for around 30 min (solution 1). In another beaker, 8 g sodium hydroxide (NaOH; ≥ 98%) was added to 40 mL DI water (solution 2). In the next step, 10 mL of solution 1 was added dropwise to solution 2 and stirred for 2 h to achieve a milky white solution. Afterward, the treated solution was dried and calcined at 450 °C for 1 h. Finally, the prepared ZnO and Ni-doped Co_3O_4 nanoparticles with a weight ratio of 80:20 were mixed manually to obtain the homogeneous ZnO/Ni-doped Co_3O_4 composites.

Sample Characterization

A field emission scanning electron microscope (FE-SEM, MIRA3, TESCAN) equipped with energy dispersive X-ray spectroscopy (FESEM-EDS) were utilized to characterize the surface morphology and constituent composition of the as-prepared products. A PANalytical X'Pert Pro diffractometer with CuKα radiation (λ=1.542 °A) at 40 kV and 30 mA was used to obtain the crystalline phase, as

well as the phase composition of the as-fabricated samples. The functional groups of the prepared samples were measured using the Fourier transform infrared spectroscopy (FTIR, Nicolet Magna 550 IR) in the wavenumber range from 400 to 4000 cm^{-1}. UV-visible diffuse reflectance spectra (UV-vis DRS) were recorded on a UV-vis V900 spectrometer in the wavelength range of 300-800 nm.

Photocatalytic decolorization process

Reactive red (RR141) dye was used to investigate the photocatalytic activity of the synthesized individual ingredients and its coupled nanostructures. The photocatalytic decolorization process was performed in a simple photoreactor (250 mL capacity) with a 400 W tungsten lamp as the light source. In a particular procedure, 50 mg of the prepared photocatalyst was added to 50 mL (10 mg/L) aqueous solution of RR141 dye. Then, the catalyst-containing solution was continuously stirred for 20 min in the dark to achieve adsorption-desorption equilibrium between the dye molecules and catalyst. At selected time intervals, 5 mL of aliquot of the mixed solution was withdrawn from the reactor and filtered for analysis through Millipore syringe filter membrane to separate the residual catalyst particulates and solution. The change in the concentration of RR141 was monitored at the corresponding wavelength with the UV-vis V900 spectrometer during the photocatalytic process. The photocatalytic decolorization efficiency (η) of the RR141 was determined according to the following formula:

$$\eta=(A_0-A_t)/A_0)100\% \quad (1)$$

where A_0 and A_t are the absorbances of the RR141 solution at the initial and each time interval of light irradiation, respectively.

RESULTS AND DISCUSSION

Materials Characterizations

SEM image and EDX pattern of ZnO/5Ni-doped Co_3O_4 nanocomposite prepared by sol-gel method are represented in Fig. 1. As displayed in Fig. 1a, nanocomposites are composed of both ZnO and Co_3O_4 nanoparticles that have a spherical morphology with a uniform size distribution and slight agglomeration. The average particle size of the nanoparticles was in the range of about 20-40 nm. EDS analysis was performed to determine the elemental composition of ZnO/5Ni-doped Co_3O_4 nanocomposite, as shown in Fig. 1b. The EDS spectrum demonstrated the existence of Zn, Co, and O and a small amount of Ni with elemental weight percentage of 46.9 % for Zn, 30.2 % for Co, 22.4 % for O, and 0.5 % for Ni. Assuming that all of the Zn atoms were bound with O as ZnO, the weight ratio of Co to O was 30:11, which was consistent with the expected formation of Co_3O_4. Thus, EDS data confirm the formation of the ZnO/5Ni-doped Co_3O_4 nanocomposite without any impurities.

Fig. 2 shows the XRD patterns of ZnO

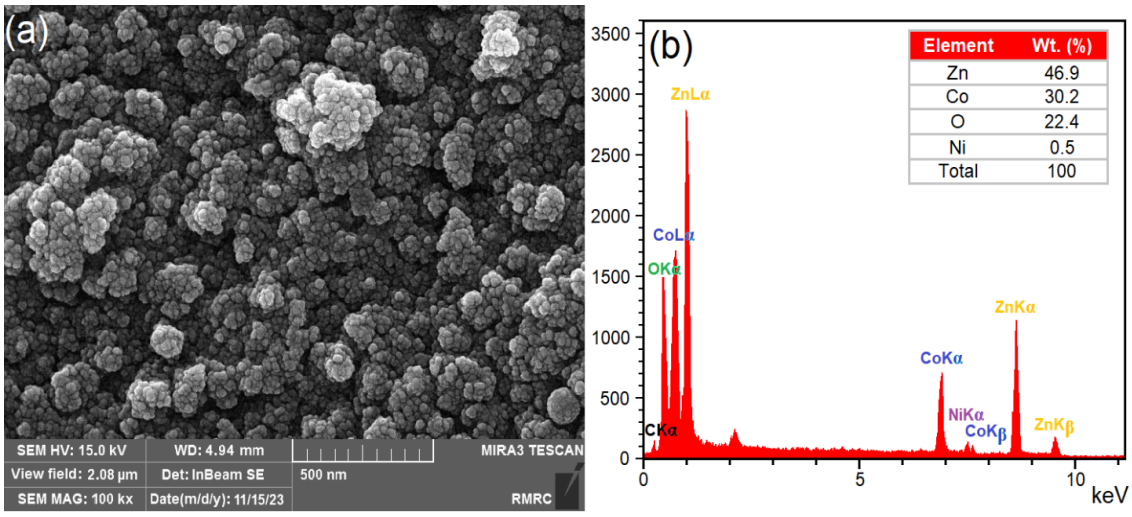

Fig. 1. (a) FE-SEM image and (b) corresponding EDS analysis of ZnO/5Ni-doped Co_3O_4 nanocomposite.

nanoparticles, Co_3O_4 nanoparticles, and ZnO/Ni-doped Co_3O_4 heterostructured nanocomposites with different amounts of Ni dopant. XRD analysis of ZnO nanoparticles reveals the main diffraction peaks at 2θ values of 31.7°, 34.4°, 36.1°, 47.5°, 56.5°, 62.9°, and 67.9°, which are attributed to the (100), (002), (101), (102), (110), (103), and (112) planes and matched with the JCPDS card No. 36-1451 of the hexagonal wurtzite structure of ZnO [29]. The apparent peaks of Co_3O_4 are of the cubic

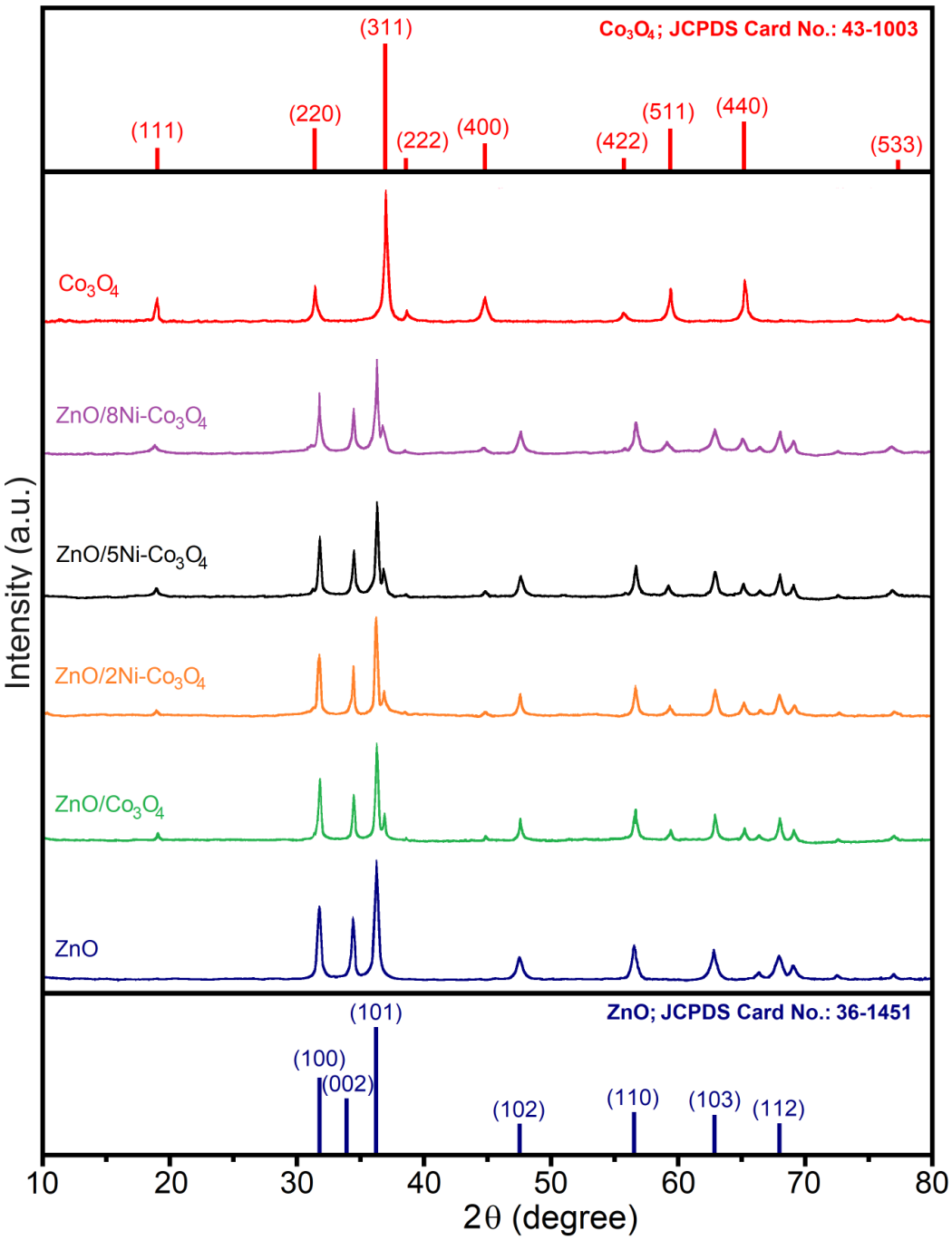

Fig. 2. XRD patterns of ZnO nanoparticles, Co_3O_4 nanoparticles, ZnO/Co_3O_4, ZnO/2Ni-Co_3O_4, ZnO/5Ni-Co_3O_4, and ZnO/8Ni-Co_3O_4 nanocomposites.

spinel type phase located at 2θ of 19.0°, 31.3°, 36.9°, 38.6°, 44.8°, 55.7°, 59.4°, 65.2°, and 77.3° corresponding to crystal planes of (111), (220), (311), (222), (400), (422), (511), (400), and (533), respectively (JCPDS card No. 043-1003) [30]. The XRD pattern of ZnO/Co_3O_4 heterojunction contains the characteristic diffraction peaks of both ZnO and Co_3O_4 materials in the nanocomposite. No impurity

Table 1. Structural parameters of pure Co_3O_4 nanoparticles and ZnO/Ni-Co_3O_4 nanocomposites.

Sample	2θ° (311)	d spacing (°A)	Lattice parameters (°A)	Crystallite size, D (°A)
Co_3O_4	36.86	2.4387	8.0882	282
ZnO/Co_3O_4	36.82	2.4413	8.0968	274
ZnO/2Ni-Co_3O_4	36.78	2.4439	8.1054	237
ZnO/5Ni-Co_3O_4	36.75	2.4458	8.1117	219
ZnO/8Ni-Co_3O_4	36.68	2.4503	8.1267	194

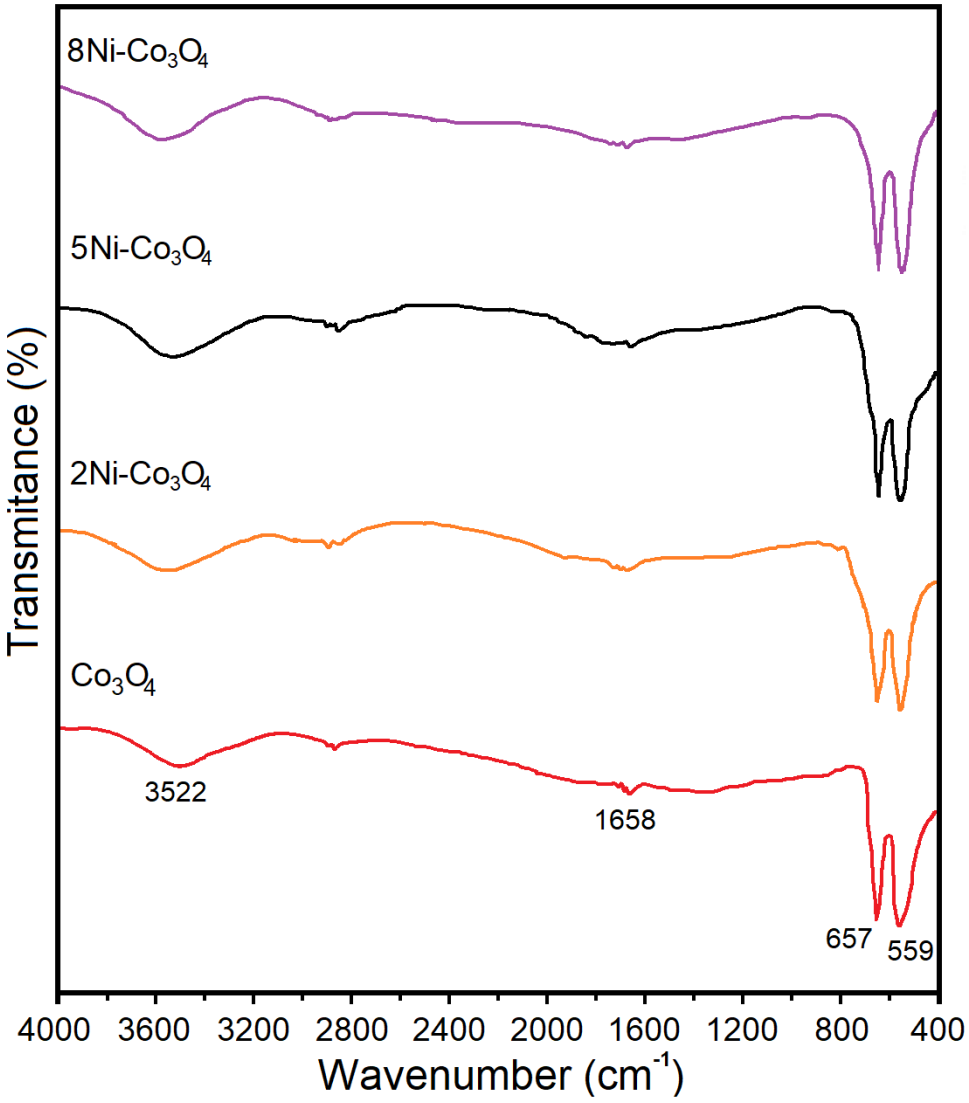

Fig. 3. FTIR spectra of Co_3O_4 and Ni-doped Co_3O_4 nanoparticle at different doping levels.

peak or no remarkable shift from the diffraction peaks of ZnO and Co_3O_4 was observed in the ZnO/Co_3O_4 sample, confirming the coexistence of ZnO and Co_3O_4 without the formation of a solid solution. In the case of ZnO/Ni-doped Co_3O_4 samples, no extra peaks associated to Ni clusters, nickel oxides

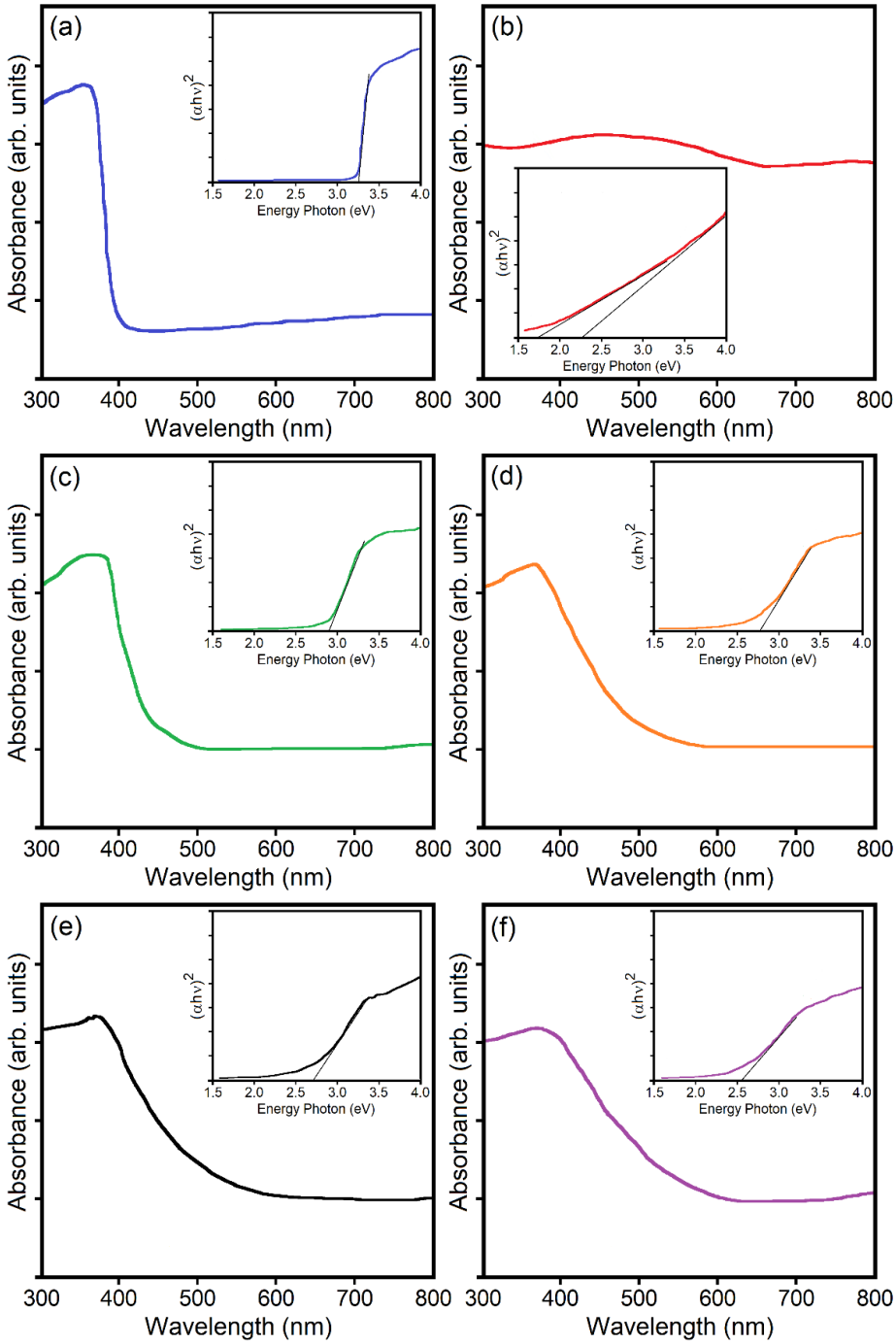

Fig. 4. UV-vis diffuse reflectance spectra (DRS) and the corresponding Tauc plots of $(\alpha h\nu)^2$ versus photon energy (hv) (inset) for the (a) pristine ZnO nanoparticles, (b) pristine Co_3O_4 nanoparticles, (c) ZnO/Co_3O_4, (d) ZnO/2Ni-Co_3O_4, (e) ZnO/5Ni-Co_3O_4, and (f) ZnO/8Ni-Co_3O_4 nanocomposites.

or other oxide phases can be observed, indicating the high purity of synthesized samples. It is also showed that the peaks of Co_3O_4 are slightly shifted towards lower diffraction angles with increasing the Ni content This suggests that the Ni ions were well incorporated into the Co sites of Co_3O_4 lattice. Further, the crystallite size and lattice parameters of Ni-doped Co_3O_4 were calculated from the XRD analysis and listed in Table 1. The data analysis indicated that there is a decrease in the values of the average crystallite size and an increase in lattice constant by increasing the Ni contents. The values of average crystallite size obtained by using the classical Debye-Scherrer formula [31] were found be 28.2 nm for Co_3O_4 nanoparticles and it decreased to 19.4 nm by increasing the Ni content steadily up to 8 wt%. The lattice parameter values for the cubic structure were determined using the following equation:

$$a = \frac{\lambda(h^2+l^2+k^2)^{1/2}}{2Sin\,\theta} \quad (2)$$

A slight increase from 8.0882 to 8.1267 °A was observed in lattice parameter of Co_3O_4 structure with doping by Ni from 0 to 8 wt%. This can be explained by the substitution of smaller Co^{2+} (0.65 °A) or Co^{3+} (0.54 °A) ions by larger Ni^{2+} ions (0.69 °A) in coordination sites [32].

FTIR data were conducted to confirm the functional groups present in Co_3O_4 and Ni-doped Co_3O_4 nanoparticles and the results are illustrated in Fig. 3. All samples exhibited the broad absorption bands around 3522 cm^{-1} and 1658 cm^{-1} are corresponds to the stretching and bending vibrations of hydroxyl groups (O-H) generated by the adsorbed water molecules. As can be clearly seen in FTIR spectra, two absorption bands were found at 559 cm^{-1} and 657 cm^{-1}, which were assigned to the stretching vibration of metal-oxygen bonding interactions (Co-O or Ni-O) within the spinel Co_3O_4 structure [33]. The first band at 559 cm^{-1} is attributed to the vibrations of Co^{3+} ions occupying the octahedral sites in the spinel structure of Co_3O_4 [34]. Similarly, the second band at 657 cm^{-1} is associated with the Co^{2+} ions in the tetrahedral sites [35]. These peaks for Ni-doped Co_3O_4 exhibited a slight shift compared to Co_3O_4 due to Ni dopant.

UV-vis DRS analysis was employed to determine the optical properties of synthesized photocatalysts. Fig. 4 shows the UV-vis spectra of ZnO nanoparticles, Co_3O_4 nanoparticles, and ZnO/Ni-doped Co_3O_4 heterostructured nanocomposites. Pristine ZnO displayed the absorbance band around 300-380 nm in the UV light region. For pristine Co_3O_4 nanoparticles was two pronounced absorption bands at 380-540 nm and 730-800 nm, which are ascribed to the ligand-to-metal charge transfer process ($O^{2-}\rightarrow Co^{2+}$ and $O^{2-}\rightarrow Co^{3+}$) in Co_3O_4 structure [30]. The absorption curves of ZnO/2Ni-Co_3O_4, ZnO/5Ni-Co_3O_4, and ZnO/8Ni-Co_3O_4 nanocomposites indicated a slightly red shift compared with pristine ZnO. It confirms that the coupling ZnO with Co_3O_4 and Ni dopant amount effects on the extended light absorption toward the visible region, suggesting

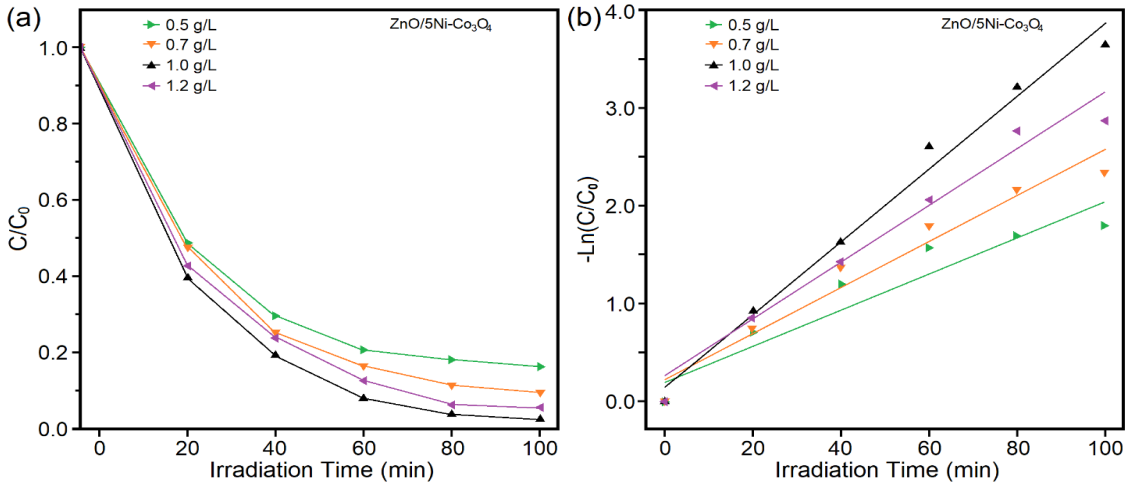

Fig. 5. (a) Effect of catalyst dosage on the photocatalytic degradation of RR141 in the presence of ZnO/5Ni-Co_3O_4 nanocomposite (dye concentration 10 mg/L), and (b) corresponding -Ln(C/C_0) versus irradiation time plots.

enhanced visible-light-driven photocatalytic activity.

Meanwhile, the optical band gap energies (E_g) are determined according to Tauc relation using Eq. (2) [36]:

$$\alpha h\upsilon = A(h\upsilon - E_g)^n \quad (3)$$

where, α is the absorption coefficient, hν is photon energy, A is constant, E_g is the bandgap energy, and n=2 for a indirectly allowed transition and n=1/2 for a directly allowed transition. Here, the best fitting gives n=1/2, indicating that the prepared photocatalysts have directly allowed electronic transitions. The band gap energies of samples were estimated by extrapolating the linear part of plots of $(\alpha h\upsilon)^2$ axis to (hν) axis at $(\alpha h\upsilon)^2=0$, as shown in the inset of Figs. 4a-f. E_g estimation from the Tauc plots yielded value of 3.25 eV for ZnO nanoparticles. For the Co_3O_4 nanoparticles, two band gap energies of 2.54 eV and 1.73 eV assigned to the charge transfer processes. It can be also found that the E_g values for ZnO/Co_3O_4, ZnO/2Ni-Co_3O_4, ZnO/5Ni-Co_3O_4, and ZnO/8Ni-Co_3O_4 nanocomposites was 2.9, 3.78, 2.71, and 2.56 eV, respectively. The optical band gap of ZnO/Co_3O_4 sample is about 0.35 eV lower than those of pristine ZnO nanoparticles, which this change may be due to the fact that the addition of Co_3O_4 adjusts the fermi energy levels across the ZnO/Co_3O_4 heterojunction [37]. Meanwhile, the incorporation of Ni into the Co_3O_4 structure gradually reduces the E_g of ZnO/Co_3O_4 nanocomposites. Ni ions contribute to generate the defects, oxygen vacancies as well as increase the number of charge carriers that leads to more conductivity of Co_3O_4 nanoparticles.

The photocatalytic activity of the produced photocatalyst materials was evaluated by the decolorization of RR141 solution under tungsten lamp irradiation. In order to study the optimum photocatalyst dosage on the photocatalytic decolorization process, different amount of ZnO/5Ni-Co_3O_4 nanocomposite were examined, while the initial dye concentration was kept constant at 10 mg/L. Fig. 5 depicts decolorization of RR141 dye with the variation in the amount of ZnO/5Ni-Co_3O_4 nanocomposite from 0.5 g/L to 1.2 g/L in the presence of tungsten lamp irradiation. It is observed that the photocatalytic decolorization efficiency and rate initially increased from 83.7% (0.0177 min^{-1}) for 0.5 g/L to 97.4% (0.0373 min^{-1}) for 1 g/L and thereafter decreases to 94.5% (0.0300 min^{-1}) for 1.2 g/L. Considering these results, 1 g/L dosage is the optimum amount of photocatalyst for the photocatalytic degradation of the dye. At catalyst concentration below this optimal value, the effective surface of catalyst is fewer available to the dye molecules and absorption of light. Increase in catalytic dosage increases the number

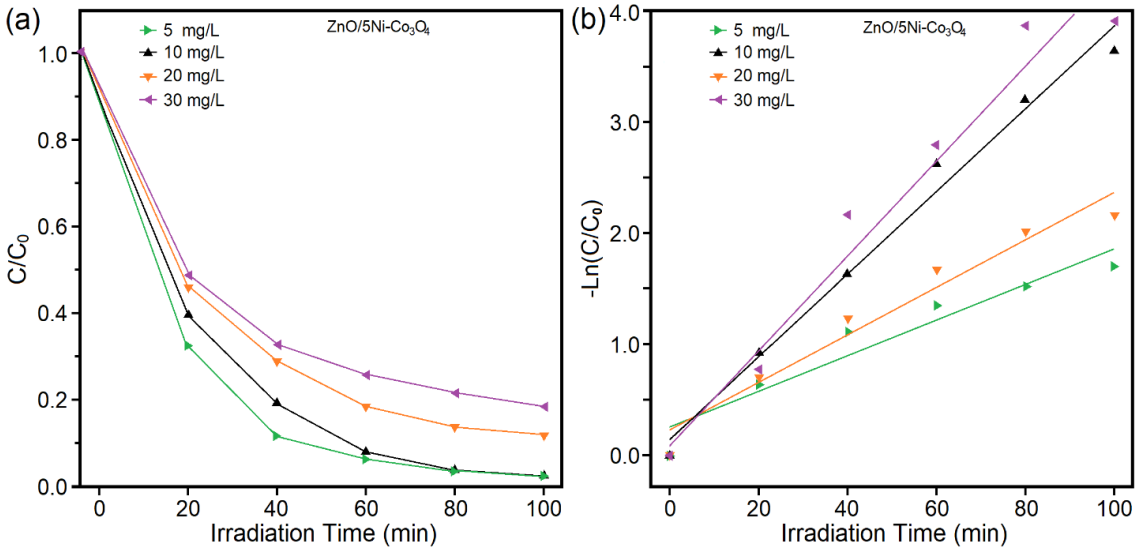

Fig. 6. (a) Effect of initial dye concentration on the photocatalytic degradation of RR 141 by using ZnO/5Ni-Co_3O_4 nanocomposite (catalyst dosage 1 g/L), and (b) corresponding -Ln(C/C_0) versus irradiation time plots.

of active sites on the surface, which results in more generation of $^{\bullet}O_2^-$ and $^{\bullet}OH$ radicals [38]. Furthermore, when the catalyst dosage exceeds above 1 g/L, a negative effect was observed in the photocatalytic efficiency of the system. This phenomenon could be explained by the light scattering and the screening effect on the surface of the photocatalyst [39].

The effect of initial dye concentration on the decolorization of RR141 by ZnO/5Ni-Co_3O_4 nanocomposite was studied with variation of dye concentrations (5,10, 20, and 30 mg/L) at constant catalyst dosage of 1 g/L. As can be seen in Fig. 6, the decolorization efficiency of RR141 was decreased from 98 to 81.8% with increasing the initial concentration of dye from 5 to 30 mg/L after 100 min. The large amount of adsorbed dye molecules on the catalyst surface leads to lack of direct contact between them, reduction of penetrated light and decreased active sites to the dye-loaded surface, causing an inhibitive role on the reaction of dye molecules with photogenerated electron/holes or reactive radicals [40].

Figs. 7a and b illustrate the plots of C/C_0 and -Ln (C/C_0) against the reaction time, respectively. It can be observed that the decolorization of

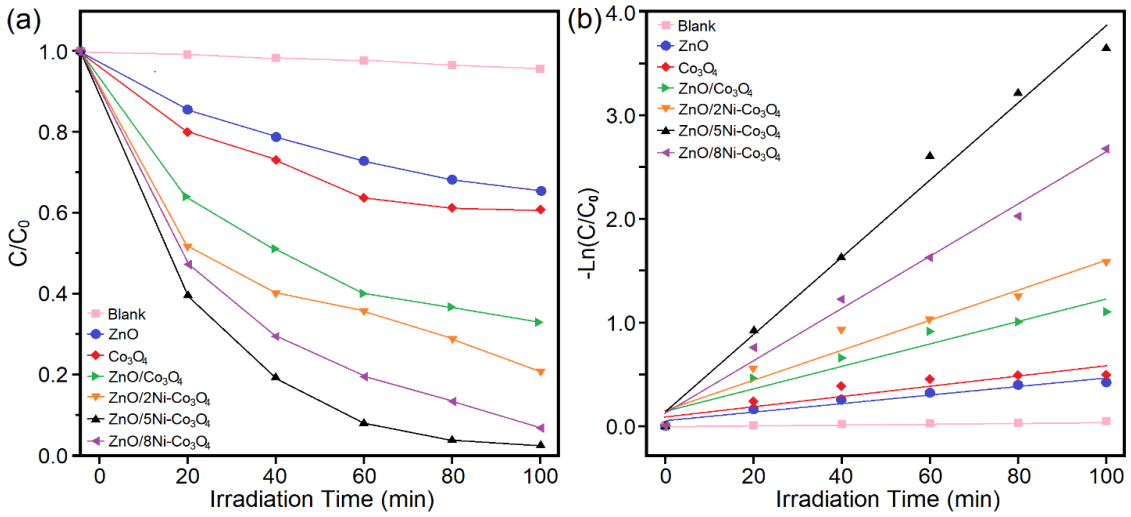

Fig. 7. (a) Concentration changes of RR141 dye solution as a function of irradiation time under tungsten lamp light, and (b) curves of -Ln(C/C_0) versus irradiation time in the presence of ZnO nanoparticles, Co_3O_4 nanoparticles, ZnO/Co_3O_4, ZnO/2Ni-Co_3O_4, ZnO/5Ni-Co_3O_4, and (f) ZnO/8Ni-Co_3O_4 nanocomposites.

Table 2. Comparison of the RR141 dye decolorization by using various photocatalysts.

Photocatalysts	Catalyst Amount	Initial Concentration	Light Source	Irradiation Time (min)	Degradation efficiency (%)	Ref.
ZnO	50 mg	10 mg/L	UV 125 W	240	95	[41]
ZnO/chitosan/CIT+2.5% ZIF composite	0.6 g/L	5 mg/L	UV-lamp (1.5 mW/cm²)	300	90.38	[42]
Zingiber/ZnO-H	50 mg	10 mg/L	UV 125 W	240	97	[43]
SDS-capped ZnO	50 mg	10 mg/L	UV 125 W	240	95	[44]
SDS-capped ZnO	50 mg	10 mg	Visible 15 W	240	60	[44]
ZnO/$BiVO_4$	50 mg	10 mg/L	UV light (mercury lamp 125 W)	240	88	[14]
Dalbergia parviflora capped ZnO	50 mg	10 mg/L	UV 125 W	30	100	[45]
ZnO/CdS	50 mg	10 mg/L	Visible 15 W	120	80	[46]
ZnO/5Ni-Co_3O_4 nanocomposite	1 g/L	10 mg/L	400 W tungsten lamp	100	97.4	This study

RR141 is resistant in the absence of irradiation. Also, the self-decolorization test confirmed that RR141 is almost no decolorization without a photocatalyst, demonstrating that the photolysis effect may be negligible. Thus, catalyst as well as light irradiation are required for efficient photocatalytic decolorization of RR141 dye. From the photocatalytic experiments, it can be found that among the synthesized photocatalysts, ZnO/5Ni-Co_3O_4 nanocomposite exhibited the best photocatalytic efficiency where 97.4% of RR141 was decolorized within 100 min of irradiation with a rate constant of 0.0373 min^{-1}. The good linearity relationship approves that the decolorization of RR141 obeys the pseudo-first-order reaction kinetics. This was then followed by ZnO/8Ni-Co_3O_4 nanocomposite where it indicated a decolorization of 93.1% with a rate constant of 0.0252 min^{-1}. The photocatalytic activity declined to 79.4% with a rate constant of 0.0144 min^{-1} when using ZnO/2Ni-Co_3O_4 nanocomposite as the photocatalyst. This values for ZnO/Co_3O_4 nanocomposite were 67.1% and 0.0107 min^{-1}, respectively. However, pristine ZnO and Co_3O_4 nanoparticles decreased 34.8% and 39.2% of RR141 within 100 min of irradiation with the rate constants of 0.0042 min^{-1} and 0.0048 min^{-1}, respectively. The high activity of nanocomposites is possibly due to the suppressed recombination of photogenerated carriers as well as the improved charge transport, which derived from the synergistic effects of Ni-doping in the Co_3O_4 lattice and its coupling with ZnO nanoparticles. The efficiency of the synthesized photocatalyst for decolorization of RR 141 dye in comparison to some recently reported ZnO based photocatalysts was also summarized in Table 2.

To examine the photocatalytic stability and reusability, the repeated experiments of RR141 decolorization the optimized ZnO/5Ni-Co_3O_4 nanocomposite were implemented for six subsequent runs in a total of 10 h. After each test, the photocatalyst was recovered through washing by distiller water and then was reused in the next run using the same conditions. As depicted in Fig. 8a, the removal efficiency decreased from 97.4% in the first cycle to 93.8% in the third run, suggesting that the prepared composite has well stability for the practical applications. Fig. 8b shows the XRD patterns of ZnO/5Ni-Co_3O_4 nanocomposite before use and after six cycling test, demonstrating tha the positions of the feature peaks before and after use are the same, and the intensities of their peaks only have a negligible decrease. It well exhibits an excellent stability of the ZnO/5Ni-Co_3O_4 photocatalyst after photocatalytic activity.

To better understand the roles of active species participated during the photocatalytic reactions, different quenching agents were added into the ZnO/5Ni-Co_3O_4 system. Benzoquinone (BQ; as a quencher of O_2^-), Isopropanol (IPA; as a quencher of OH^-) and Triethanolamine (TEA; as a quencher of h^+) were respectively used under the same conditions with photocatalytic decolorization experiments. Fig. 9 presents the

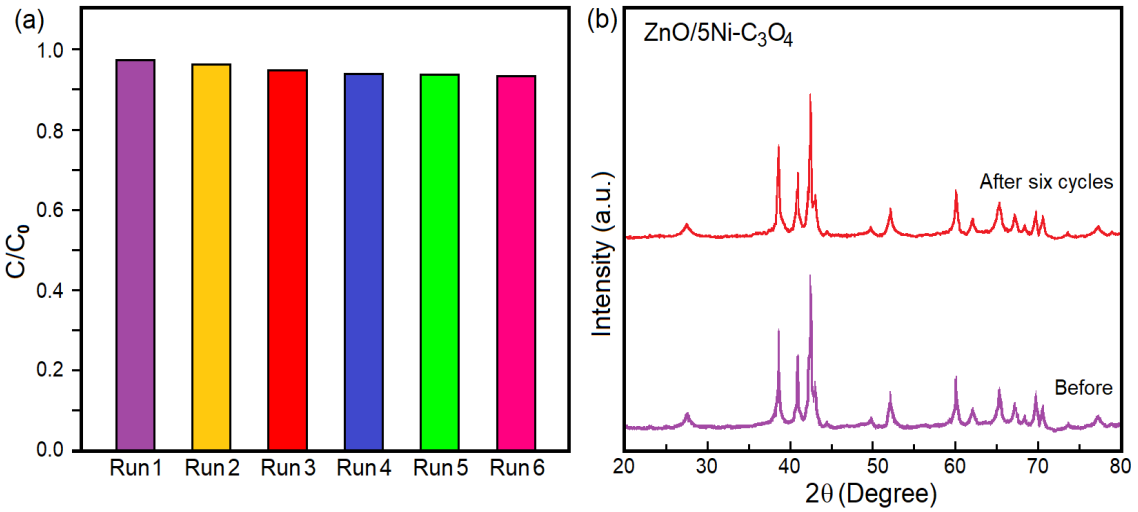

Fig. 8. (a) Reusability of ZnO/5Ni-Co_3O_4 nanocomposite for RR141 decolorization for six cycles. (b) XRD analysis of ZnO/5Ni-Co_3O_4 nanocomposite before and after use.

photocatalytic efficiency of RR141 over ZnO/5Ni-Co_3O_4 heterostructure was 79, 33.9, and 55.4% with TEA, IPA and BQ, respectively. These results suggest that hydroxyl radicals play more important role in RR141 decolorization process, compared to the photo-generated superoxide ($^{\bullet}O_2^-$) radicals and holes.

Based on the above-mentioned results, a probable mechanism of the decolorization via ZnO/Ni-doped Co_3O_4 heterojunction was proposed and illustrated in Fig. 10. ZnO is an n-type semiconductor and Co_3O_4 is known as a p-type semiconductor. The Fermi level of the n-type ZnO is located near the conduction band (CB), while that of p-type Co_3O_4 is located near the valence band (VB). The CB and VB potentials of semiconductor materials can be estimated using following relations [47]:

$$E_{CB} = \chi - E^0 - 0.5E_g \quad (4)$$

$$E_{VB} = E_{CB} + E_g \quad (5)$$

where E_{CB} and E_{VB} are the potentials of the conduction and valence band edge, χ is defined as the absolute electronegativity of constituent atoms, E^0 is the energy of free electrons on the hydrogen scale (about 4.5 eV), which the χ values for ZnO and Co_3O_4 are 5.79 eV [9] and 5.90 eV [48], respectively, and E_g is band gap of the photocatalyst. Ni doping into Co_3O_4 lattice can induce additional mid-gap energy levels just below the CB edge, which creates photogenerated electron-trapping sites [49]. After contact, the Fermi levels of the two components reaches a thermodynamic equilibrium which leads to create an electric field in the Interface of n-p ZnO/Co_3O_4 heterojunction and shift the band positions in the two components. Thus, the band positions of the Co_3O_4 is up shifted beyond the band positions of ZnO according to type-II band gap configuration. Therefore, it can be concluded that the Ni doping in the Co_3O_4 structure along with its coupling with ZnO serve to separate the charge carriers, resulting in the enhanced photocatalytic activity. Under light irradiation, both ZnO and Co_3O_4 can be excited, and photo-generated electrons move from the CB of Co_3O_4 to that of ZnO. This electrons on the CB of ZnO were trapped by molecular oxygen to form $^{\bullet}O_2^-$ radicals, while the photo-generated holes migrated from the VB of ZnO to that of Co_3O_4 react with hydroxyl ions (OH^-) to form $^{\bullet}OH$ radicals. These free radicals are strong oxidizing agents to decompose dye molecules.

$$ZnO/Ni\text{-}Co_3O_4 + hv \rightarrow ZnO/Ni\text{-}Co_3O_4\ (e^-_{CB} + h^+_{VB}) \quad (6)$$

$$Ni\text{-}Co_3O_4\ (e^-_{CB}) + ZnO \rightarrow ZnO\ (e^-_{CB}) \quad (7)$$

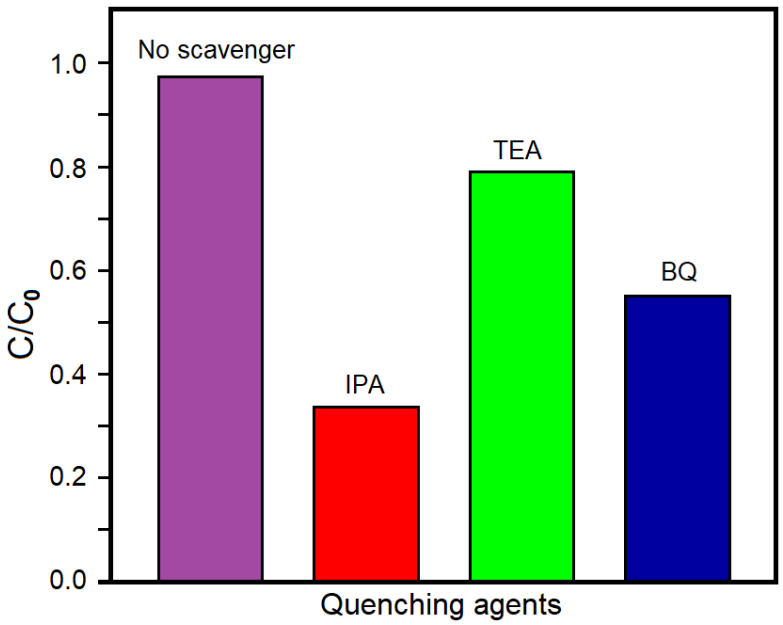

Fig. 9. Influence of the different scavengers on the RR141 decolorization by ZnO/5Ni-Co_3O_4 nanocomposite.

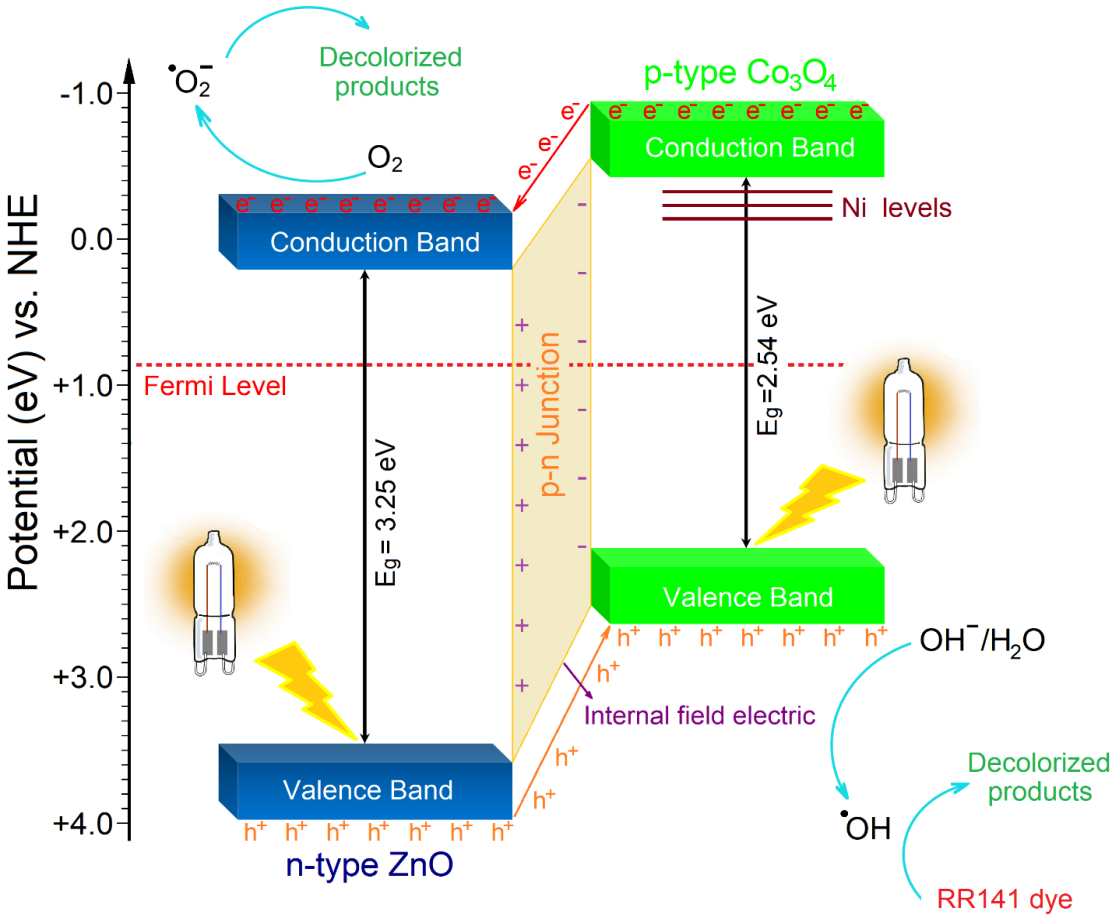

Fig. 10. Schematic illustration of the band diagram and photocatalytic mechanism of ZnO/Ni-doped Co_3O_4 heterojunction.

$$ZnO\ (h^+_{VB}) + Ni\text{-}Co_3O_4 \rightarrow Ni\text{-}Co_3O_4\ (h^+_{VB}) \quad (8)$$

$$O_2 + ZnO\ (e^-_{CB}) \rightarrow \bullet O_2^- \quad (9)$$

$$Ni\text{-}Co_3O_4\ (h^+_{VB}) + H_2O\ (ads) \rightarrow \bullet OH + H^+ \quad (10)$$

$$Ni\text{-}Co_3O_4\ (h^+_{VB}) + OH^-\ (ads) \rightarrow \bullet OH \quad (11)$$

$$\bullet O_2^- + H^+ \rightarrow \bullet HO_2 \quad (12)$$

$$\bullet HO_2 + \bullet HO_2 \rightarrow H_2O_2 + O_2 \quad (13)$$

$$H_2O_2 + e^- \rightarrow \bullet OH + OH^- \quad (14)$$

$$\bullet O_2^- + \bullet OH + h^+ + RR141\ dye\ molecules \rightarrow decolorized\ products \quad (15)$$

CONCLUSION

In summary, a type-II band alignment heterojunction of ZnO/Ni-doped Co_3O_4 nanocomposites with different amounts of Ni dopant has successfully fabricated via sol-gel method, and the resultant photocatalysts demonstrated a significant enhancement and stability in photocatalytic decolorization efficiency of RR141 dye. The photocatalytic results revealed a maximum decolorization performance of 97.4% with a rate constant of 0.0373 min^{-1} after 100 min light irradiation. The prepared nanocomposites exhibited outstanding stability even after six cycles, which confirms their potential for reuse and long-term practical applications in the environmental field.

CONFLICT OF INTEREST

The authors declare that there is no conflict of interests regarding the publication of this

manuscript.

REFERENCES

1. Tkaczyk A, Mitrowska K, Posyniak A. Synthetic organic dyes as contaminants of the aquatic environment and their implications for ecosystems: A review. Science of The Total Environment. 2020;717:137222.
2. Al-Tohamy R, Ali SS, Li F, Okasha KM, Mahmoud YAG, Elsamahy T, et al. A critical review on the treatment of dye-containing wastewater: Ecotoxicological and health concerns of textile dyes and possible remediation approaches for environmental safety. Ecotoxicology and Environmental Safety. 2022;231:113160.
3. Zazycki MA, Godinho M, Perondi D, Foletto EL, Collazzo GC, Dotto GL. New biochar from pecan nutshells as an alternative adsorbent for removing reactive red 141 from aqueous solutions. Journal of Cleaner Production. 2018;171:57-65.
4. Ruscasso F, Bezus B, Garmendia G, Vero S, Curutchet G, Cavello I, Cavalitto S. Debaryomyces hansenii F39A as biosorbent for textile dye removal. Rev Argent Microbiol. 2021;53(3):257-265.
5. Behloul H, Ferkous H, Bougdah N, Djellali S, Alam M, Djilani C, et al. New insights on the adsorption of CI-Reactive Red 141 dye using activated carbon prepared from the ZnCl2-treated waste cotton fibers: Statistical physics, DFT, COSMO-RS, and AIM studies. J Mol Liq. 2022;364:119956.
6. Yaman C, Gündüz G. A parametric study on the decolorization and mineralization of C.I. Reactive Red 141 in water by heterogeneous Fenton-like oxidation over FeZSM-5 zeolite. Journal of environmental health science & engineering. 2015;13:7-7.
7. Sansenya T, Masri N, Chankhanittha T, Senasu T, Piriyanon J, Mukdasai S, Nanan S. Hydrothermal synthesis of ZnO photocatalyst for detoxification of anionic azo dyes and antibiotic. Journal of Physics and Chemistry of Solids. 2022;160:110353.
8. Mahroudi A, Aghasi M, Dolatabadi M, Ahmadzadeh S. Removal of reactive blue 171 dye from aqueous solution and textile industrial wastewater using peroxi-electrocoagulation process by iron electrode: application of response surface methodology. Desalination and Water Treatment. 2022;272:266-276.
9. Qutub N, Singh P, Sabir S, Sagadevan S, Oh W-C. Enhanced photocatalytic degradation of Acid Blue dye using CdS/TiO_2 nanocomposite. Sci Rep. 2022;12(1):5759-5759.
10. Sun C, Yang J, Xu M, Cui Y, Ren W, Zhang J, et al. Recent intensification strategies of SnO_2-based photocatalysts: A review. Chem Eng J. 2022;427:131564.
11. Frizzo MS, Betega K, Poffo CM, Falk GS, Hotza D, Rodrigues Neto JB. Highly enhanced adsorption and photocatalytic performance of TiO_2 quantum dots synthesized by microwaves for degradation of reactive red azo dye. Journal of Nanoparticle Research. 2021;23(5).
12. Singh K, Nancy, Bhattu M, Singh G, Mubarak NM, Singh J. Light-absorption-driven photocatalysis and antimicrobial potential of PVP-capped zinc oxide nanoparticles. Sci Rep. 2023;13(1):13886-13886.
13. Kafian S, Sadeghzadeh-Attar A. Photocatalytic degradation of Basic Blue 41 dye under visible light over $SrTiO_3$/Ag_3PO_4 hetero-nanostructures. International Journal of Applied Ceramic Technology. 2022;19(6):3347-3357.
14. Wannakan K, Khansamrit K, Senasu T, Nanan S. Ultrasound-Assisted Synthesis of a ZnO/$BiVO_4$ S-Scheme Heterojunction Photocatalyst for Degradation of the Reactive Red 141 Dye and Oxytetracycline Antibiotic. ACS omega. 2023;8(5):4835-4852.
15. Raha S, Ahmaruzzaman M. ZnO nanostructured materials and their potential applications: progress, challenges and perspectives. Nanoscale advances. 2022;4(8):1868-1925.
16. Al-Mamun MR, Iqbal Rokon MZ, Rahim MA, Hossain MI, Islam MS, Ali MR, et al. Enhanced photocatalytic activity of Cu and Ni-doped ZnO nanostructures: A comparative study of methyl orange dye degradation in aqueous solution. Heliyon. 2023;9(6):e16506-e16506.
17. Pascariu P, Olaru N, Rotaru A, Airinei A. Innovative Low-Cost Carbon/ZnO Hybrid Materials with Enhanced Photocatalytic Activity towards Organic Pollutant Dyes' Removal. Nanomaterials (Basel, Switzerland). 2020;10(9):1873.
18. Al Ghafry SSA, Al-Abri MZ, Al Farsi B, Al Marzouqi F, Al Farsi LM, Roslan NA, Supangat A. Ga-doped ZnO nanorods: The photocatalytic performance of methylene blue under solar irradiation. Optical Materials. 2022;126:112139.
19. Abebe B, Murthy HCA, Amare E. Enhancing the photocatalytic efficiency of ZnO: Defects, heterojunction, and optimization. Environmental Nanotechnology, Monitoring & Management. 2020;14:100336.
20. Wei Y, Shahid MZ, Lyu S, Sun W, Lyu S. One-pot, ligand-free, room-temperature synthesis of Au/Pd/ZnO nanoclusters with ultra-low noble metal loading and synergistically improved photocatalytic performances. RSC advances. 2021;11(37):22618-22624.
21. Ujjan ZA, Bhatti MA, Shah AA, Tahira A, Shaikh NM, Kumar S, et al. Simultaneous doping of sulfur and chloride ions into ZnO nanorods for improved photocatalytic properties towards degradation of methylene blue. Ceram Int. 2022;48(4):5535-5545.
22. Lei X, Cao Y, Chen Q, Ao X, Fang Y, Liu B. ZIF-8 derived hollow CuO/ZnO material for study of enhanced photocatalytic performance. Colloids Surf Physicochem Eng Aspects. 2019;568:1-10.
23. Ishfaq M, Hassan W, Sabir M, Somaily HH, Hachim SK, Kadhim ZJ, et al. Wet-chemical synthesis of ZnO/CdO/CeO_2 heterostructure: A novel material for environmental remediation application. Ceram Int. 2022;48(23):34590-34601.
24. Tien T-M, Chen EL. A Novel ZnO/Co3O4 Nanoparticle for Enhanced Photocatalytic Hydrogen Evolution under Visible Light Irradiation. Catalysts. 2023;13(5):852.
25. Subagyo R, Yudhowijoyo A, Sholeha NA, Hutagalung SS, Prasetyoko D, Birowosuto MD, et al. Recent advances of modification effect in Co_3O_4-based catalyst towards highly efficient photocatalysis. Journal of Colloid and Interface Science. 2023;650:1550-1590.
26. Zeid EFA, Obiedallah FM, Abu-Sehly A-H, Mohamed WAA, El-Aal MA. A comparative study of single and bi-doped Co_3O_4 nanocatalysts for the photodegradation of methyl orange dye. Journal of Molecular Structure. 2023;1293:136203.
27. Keerthana SP, Yuvakkumar R, Kumar PS, Ravi G, Vo D-VN, Velauthapillai D. Influence of tin (Sn) doping on Co3O4 for enhanced photocatalytic dye degradation. Chemosphere. 2021;277:130325.
28. Fida M, Iqbal S, Shah M, Fazal T, Ismail B, Rehman Hu, et al. Mn^{2+} Doped Cobalt Oxide and Its Composite with Carbon Nanotubes for Adsorption-Assisted Photocatalytic

Applications. Sustainability. 2022;14(24):16932.
29. Josun J, Sharma P, Kumar Garg V. Optical and structural behavior of hydrothermally synthesized ZnO nanoparticles at various temperatures with NaOH molar ratios. Results in Optics. 2024;14:100601.
30. Yousefi S, Sadeghzadeh-Attar A. Coupling effect of Fe-doped Co_3O_4 nanoparticles with $SrTiO_3$ nanotubes on the high-efficiency photocatalytic activities of basic violet 16 dye degradation and H_2 evolution. Inorg Chem Commun. 2024;162:112273.
31. Sadeghzadeh-Attar A, Bafandeh MR. Effect of annealing on UV-visible absorption and photoluminescence behavior of liquid phase deposited TiO_2 nanorods. International Journal of Applied Ceramic Technology. 2019;16(6):2429-2440.
32. Cardenas Flechas LJ, Xuriguera Martín E, Padilla Sanchez JA, Chimenos Ribera JM, Rincón Joya M. Experimental comparison of the effect of temperature on the vibrational and morphological properties of $Ni_xCo_{3-x}O_4$ nanostructures. Materials Letters. 2021;303:130477.
33. Silambarasan S, Sivakumar M, Kumar KR, Jiang Z, Maiyalagan T. Nickel-doped Co_3O_4 spinel nanospheres embedded in nitrogen-doped carbon composites derived from bimetallic NiCo metal–organic framework as a high-performance asymmetric supercapacitor. New Journal of Chemistry. 2023;47(18):8649-8660.
34. Worku AK, Asfaw A, Ayele DW. Engineering of Co_3O_4 electrode via Ni and Cu-doping for supercapacitor application. Frontiers in chemistry. 2024;12:1357127-1357127.
35. Karthikeyan A, Mariappan R, Krishnamoorthy E, Bakkiyaraj R. Effect of Nickel doping on Cobalt Oxide nanoparticles for energy storage applications. Ionics. 2024;30(4):2069-2082.
36. Sadeghzadeh-Attar A, Akhavan-Safaei I, Bafandeh MR. UV-visible absorption and photoluminescence characteristics of SnO_2 nano-tube/wire arrays fabricated by LPD method. International Journal of Applied Ceramic Technology. 2018;15(5):1084-1094.
37. Markhabayeva AA, Kalkozova ZK, Nemkayeva R, Yerlanuly Y, Anarova AS, Tulegenova MA, et al. Construction of a ZnO Heterogeneous Structure Using Co_3O_4 as a Co-Catalyst to Enhance Photoelectrochemical Performance. Materials (Basel, Switzerland). 2023;17(1):146.
38. Ajibade PA, Oluwalana AE, Andrew FP. Morphological Studies, Photocatalytic Activity, and Electrochemistry of Platinum Disulfide Nanoparticles from Bis(morpholinyl-4-carbodithioato)-platinum(II). ACS omega. 2020;5(42):27142-27153.
39. Sakhaei F, Salahi E, Olya ME, Mobasherpour I. Synthesis, characterization and application of pH-sensitive $CoFe_2O_4$/reduced graphene oxide (RGO) nanocomposite in a circulated photocatalytic reactor for Reactive Red 141 removal of wastewaters. Res Chem Intermed. 2017;43(7):4063-4078.
40. Kushare SS, Bobade VD, Tope DR, Borhade AV. $CoCr_2O_4$@GeO_2@ZnO core-shell nanoparticle as a novel recoverable catalyst: Preparation, characterization and photocatalytic degradation of basic fuchsin dye. J Indian Chem Soc. 2021;98(12):100239.
41. Chankhanittha T, Nanan S. Hydrothermal synthesis, characterization and enhanced photocatalytic performance of ZnO toward degradation of organic azo dye. Materials Letters. 2018;226:79-82.
42. Phonlakan K, Khamsuk B, Soontonhong N, Panawong C, Kongseng P, Chantarak S, Budsombat S. Composite beads from chitosan and zeolitic imidazolate framework-8 for the adsorption and photocatalytic degradation of reactive red 141. RSC advances. 2023;13(18):12295-12308.
43. Nugroho D, Wannakan K, Nanan S, Benchawattananon R. Hydrothermal synthesis of Zingiber/ZnO for enhanced photodegradation of ofloxacin antibiotic and reactive red azo dye (RR141). PLoS One. 2024;19(5):e0300402-e0300402.
44. Kakarndee S, Nanan S. SDS capped and PVA capped ZnO nanostructures with high photocatalytic performance toward photodegradation of reactive red (RR141) azo dye. Journal of Environmental Chemical Engineering. 2018;6(1):74-94.
45. Chankhanittha T, Yenjai C, Nanan S. Utilization of formononetin and pinocembrin from stem extract of Dalbergia parviflora as capping agents for preparation of ZnO photocatalysts for degradation of RR141 azo dye and ofloxacin antibiotic. Catal Today. 2022;384-386:279-293.
46. Senasu T, Chankhanittha T, Hemavibool K, Nanan S. Visible-light-responsive photocatalyst based on ZnO/CdS nanocomposite for photodegradation of reactive red azo dye and ofloxacin antibiotic. Mater Sci Semicond Process. 2021;123:105558.
47. Niknam H, Sadeghzadeh-Attar A. Constructing trinary heterostructure of TiO_2/$CoCr_2O_4$/$SrTiO_3$ to enhance photocatalytic activity toward degradation of yellow 28 dye. Materials Chemistry and Physics. 2023;299:127489.
48. Shanmugasundaram E, Vellaisamy K, Ganesan V, Narayanan V, Saleh Ni, Thambusamy S. Dual Applications of Cobalt-Oxide-Grafted Carbon Quantum Dot Nanocomposite for Two Electrode Asymmetric Supercapacitors and Photocatalytic Behavior. ACS omega. 2024;9(12):14101-14117.
49. Didari J, Sadeghzadeh-Attar A. Ni-N codoped SnO_2/Fe_2O_3 nanocomposite as advanced bifunctional photocatalyst for simultaneous photocatalytic redox conversion of Cr(VI) and As(III). Journal of the Taiwan Institute of Chemical Engineers. 2021;119:232-244.